Exploring the Binding of Barbital to a Synthetic Macrocyclic Receptor; a Charge Density Study†

Jonathan J. Du,[1] Jane R. Hanrahan,[1] V. Raja Solomon,[1] Peter A. Williams,[1,4] Paul W. Groundwater,[1] Jacob Overgaard,[3] James A. Platts[2] and David E. Hibbs[1]*

[1]*Faculty of Pharmacy, University of Sydney, NSW 2006 Australia*

[2]*School of Chemistry, Cardiff University, Cardiff, CF10 3AT, UK.*

[3]*Department of Chemistry, Center for Materials Crystallography, Aarhus University, Langelandsgade 140, Aarhus C, 8000, Denmark*

[4]*School of Science and Health, Western Sydney University, Locked Bag 1797, Penrith, NSW, 2751*

**Corresponding author: David E. Hibbs,* david.hibbs@sydney.edu.au

†Electronic supplementary information (ES) available. CCDC 1562106, 1562107 and 1562108. For ESI and crystallographic data in CIF or other electronic formats, see DOI: XXXXXXX

Abstract

Experimental charge density distribution studies, complemented by quantum mechanical theoretical calculations, of a host-guest system comprised of a macrocycle (**1**) and barbital (**2**) in a 1:1 ratio (**3**) have been carried out *via* high resolution single crystal X-ray diffraction. The data was modelled using the conventional multipole model of electron density according to the Hansen-Coppens formalism. The asymmetric unit of macrocycle (**1**) contained an intraannular ethanol molecule and an extraannular acetonitrile molecule, while the asymmetric unit of (**3**) also contained an intraannular ethanol molecule. Visual comparison of the conformations of the macrocyclic ring shows the rotation by 180° of an amide bond attributed to competitive hydrogen bonding. It was found the intraannular and extraannular molecules inside were orientated to maximise the number of hydrogen bonds present, with the presence of barbital in (**3**) resulting in the greatest stabilisation. Hydrogen bonds ranging in strength from 4-70 kJ mol^{-1} were the main stabilising force. Further analysis of the electrostatic potential between (**1**), (**2**) and (**3**) showed significant charge redistribution when co-crystallisation occurred, which was further confirmed by a comparison of atomic charges. The findings presented herein introduce the possibility of high resolution X-ray crystallography playing a more prominent role in the drug design process.

Introduction

The potential medicinal applications of macrocycles (containing rings composed of eight or twelve or more atoms depending on the reference[1-2]) have been largely ignored due to the belief that their properties were not on the drug like spectrum *i.e.* they had low target selectivity, were poorly absorbed and did not obey Lipinski's Rule of Five[3]. Recently, interest in these molecules in medicine has been rekindled with potential applications as artificial receptors, drug delivery vehicles, enzyme inhibitors,[2] or as potential detoxification routes. The main attraction of these molecules lies in their diversity, allowing each one to be tailored towards a specific target in terms of size, lipophilicity or hydrophilicity, molecular recognition and myriad other physicochemical properties[4].

All the potential applications mentioned above involve the formation of binary, ternary or even higher order systems consisting of the macrocycle and one or more target molecules. In the context of these applications, it is imperative that these systems form preferentially over other interactions and complexes which might occur. These systems are reliant on weak interactions such as hydrogen bonds, van der Waals and π-π stacking forces to drive their formation and stability. As such, a greater understanding of these interactions is required for these macrocycles to become viable therapeutic options in modern medicine. Nguyen *et al.* recently published work in this area, using density functional theory (DFT) and atoms in molecules (AIM) theory to map the electron density distribution (EDD) in biologically significant host-receptor complexes.[5-6] The conclusion drawn from these studies was that improved understanding of electron and energy distribution within these systems will lead to improvements in the drug design and development pipeline, resulting in less toxic and improved therapeutic options.

Chang *et al.* have previously described the synthesis of macrocycles which were then used as an artificial receptor for diethylbarbituric acid **(2)** [5,5-diethyl-(1*H*,3*H*,5*H*)-pyrimidine-2,4,6-trione; barbital][4]. Barbital, belongs to a class of relatively old drugs previously used to relieve anxiety and insomnia and currently used as anticonvulsants and in anaesthesia. Barbiturates have now been superseded by the benzodiazepines which have an improved safety profile, however, this model provides an excellent starting point to gain an improved understanding of the binding interactions and energy states of the molecules in these complexes.

High resolution X-ray crystallography has been used with great success to obtain experimental EDD's for many molecules and systems as seen through the myriad publications in the field[5-10]. Topological analysis of the obtained EDD allows information regarding the presence and nature of weak interactions to be extracted and analysed to gain an improved understanding of the changes in electron density redistribution which occur upon the formation of weak interactions. Readers are referred to an excellent review by Koritsanszky *et al.*[11] for more information. Here, we present an analysis of the 14,16-dioxa-2,6,8,22-tetraaza-1,7(2,6)-dipyridina-15(2,7)-naphthalena-4(1,3)-benzenacyclodocosaphane-3,5,9,21-tetraone **(1)** complexed with barbital **(2)** developed by Chang *et al.*[4] and its constituent molecules at the electronic level, through the use of single crystal X-ray diffraction to map the EDD within the system and to understand the nature of the binding interactions which drive the formation and stability of this system (including the bond strength of these systems). ORTEP diagrams of the three systems studied can be found in Figures 1-3. Previous studies have examined the charge density distribution of barbital alone,[12] however no studies of this nature have been performed on the macrocyclic compound or on these co-crystal systems.

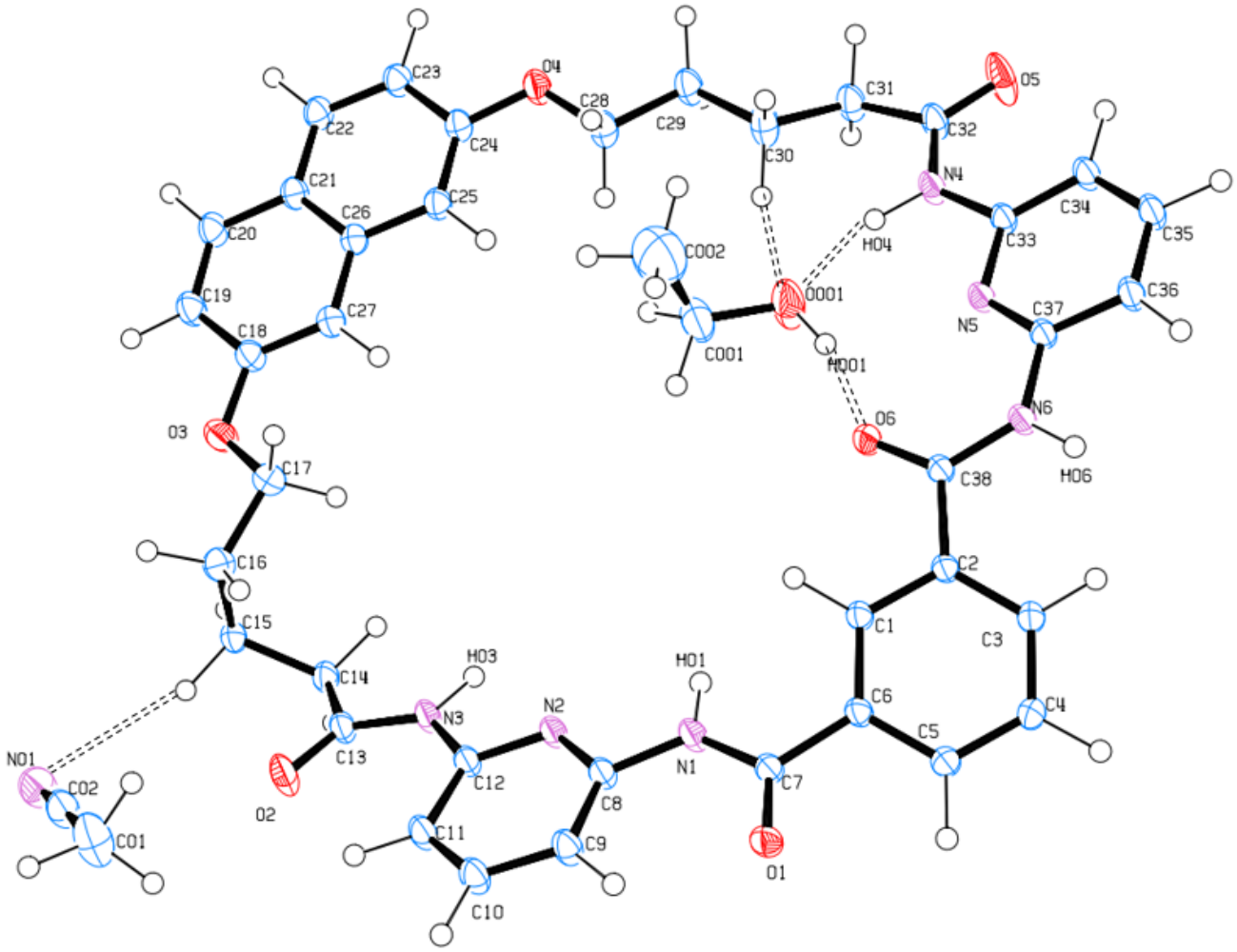

Figure 1: ORTEP diagram of macrocycle (**1**). Thermal ellipsoids are shown at 50% probability.

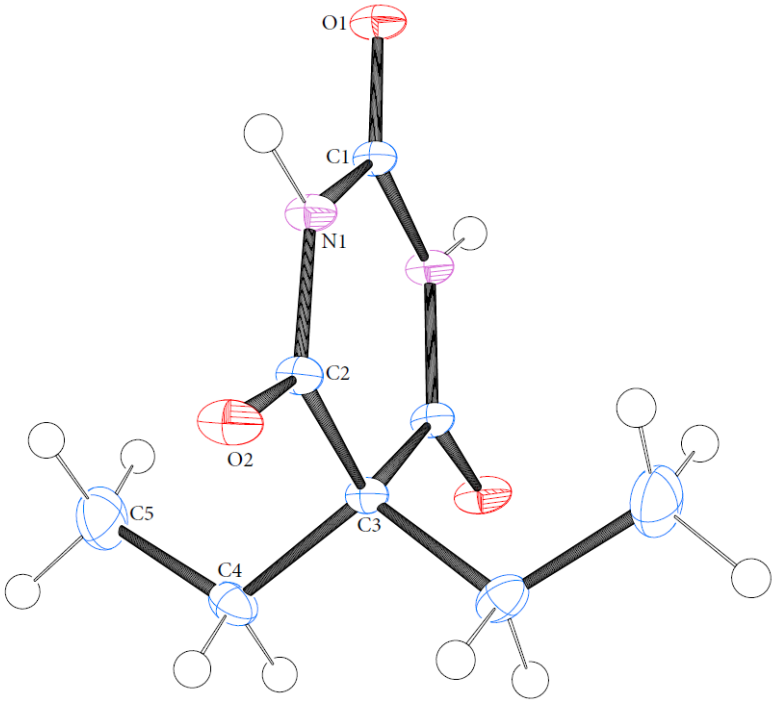

Figure 2: ORTEP diagram of barbital (**2**). Thermal ellipsoids are shown at 50% probability.

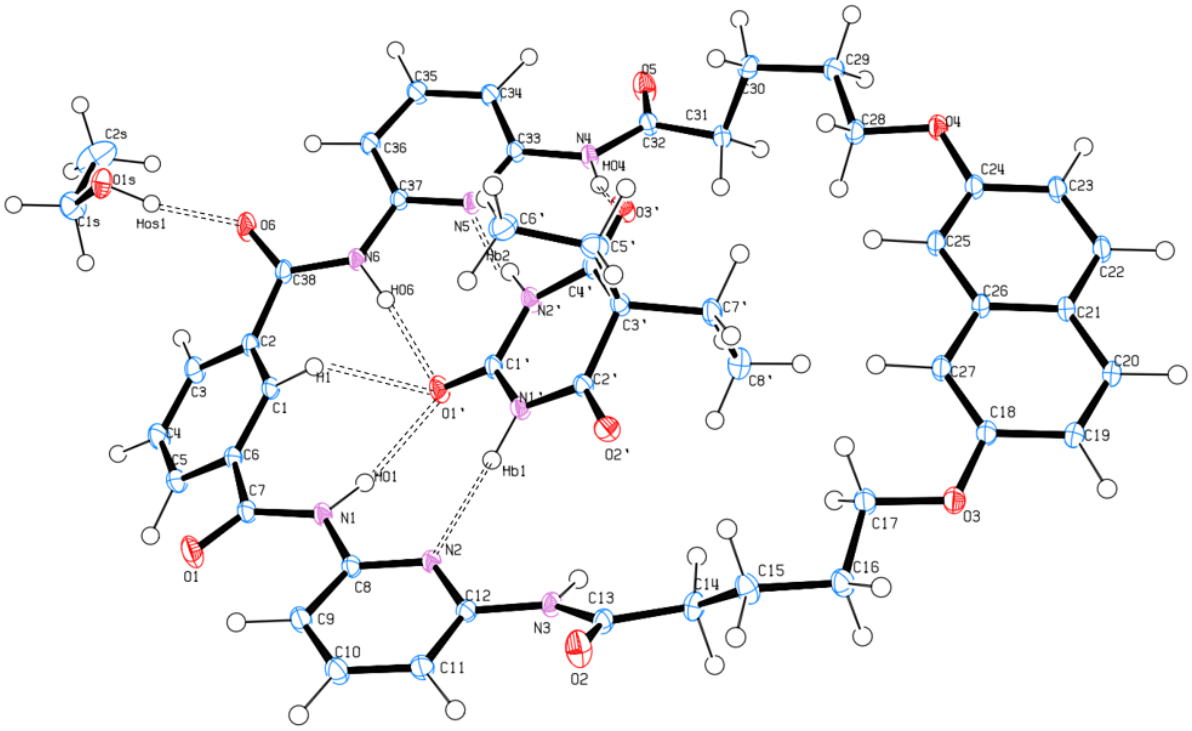

Figure 3: ORTEP diagram of macrocycle-barbital complex (**3**). Thermal ellipsoids are shown at 50% probability.

Method

All chemicals were purchased from Sigma-Aldrich (St. Louis, MO) at the highest grade available and used without further purification. (**1**) was synthesised as previously reported by Chang et al.[4]. The synthetic route can be found in Scheme 1. Spectroscopic details can be found in the supplementary information. (**1**) and (**2**) were crystallised *via* slow evaporation in ethanol. (**3**) was formed *via* dissolving equimolar amounts of (**1**) and (**2**) in ethanol and left at room temperature for slow evaporation.

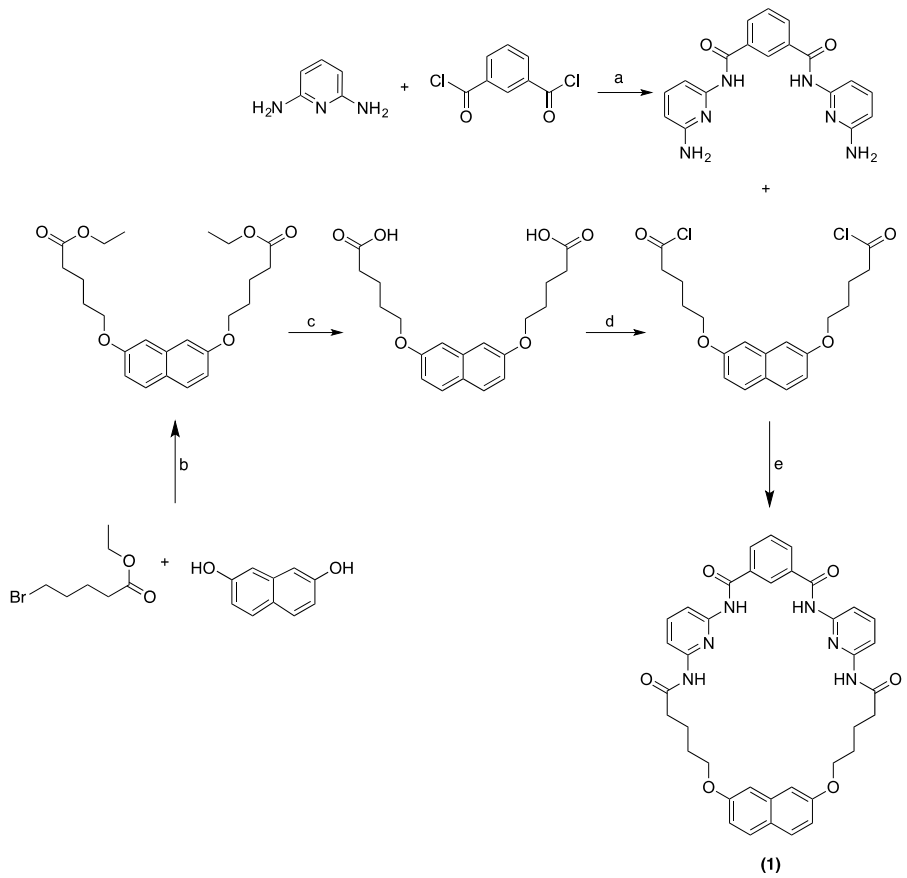

Reagents and conditions: (a) THF, RT, 4h; (b) K_2CO_3, Acetone, reflux 24h; (c) 10% aq. NaOH, EtOH, reflux 24h; (d) oxalyl chlride, 2^{-3} drops DMF, DCM, RT; (e) THF, RT, 4h.

Scheme 1: Synthetic route for 14,16-dioxa-2,6,8,22-tetraaza-1,7(2,6)-dipyridina-15(2,7)-naphthalena-4(1,3)-benzenacyclodocosaphane-3,5,9,21-tetraone.

Data Collection, Integration and Reduction

Single-crystal X-ray diffraction experiments were carried out in the Faculty of Pharmacy at the University of Sydney using an Rigaku SuperNova™ X-ray diffractometer with an X-ray wavelength of 0.7107 Å (Mo*K*α) at 150K. Crystals of (**1**), (**2**) and (**3**) with dimensions (0.3 x 0.2 x 0.25) mm, (0.25 x 0.3 x 0.25) mm and (0.2 x 0.25 x 0.25) mm, respectively, were mounted on thin glass fibres with Paratone-N oil being used as both adhesive and cryoprotectant. Data were collected for all crystals using 1° ω scans maintaining the crystal-to-detector distance at 5.3 cm for (**1**), (**2**) and (**3**). For (**1**), (**2**) reciprocal space

coverage was achieved during the data collection by positioning the detector arm at two different angles in 2θ, at 41.6° and 90.5°. For these angle settings, exposure times of 30 and 90 seconds were used for (**1**) and 15 and 60 seconds for (**2**). Reciprocal space was covered in (**3**) *via* positioning the detector arm at 41.2° and 90.5° in 2θ, with exposure times of 15 and 50 seconds per frame, respectively. A total of 2389, 4021 and 7604 frames were collected for (**1**), (**2**) and (**3**) respectively.

Integration and reduction of the collected data were performed with the CrysAlis^{Pro} software package[13]. All crystals were cooled to 150K with an Oxford Cryosystems COBRA cooler. The unit cell parameters for (**1**) were refined from 291974 reflections in the monoclinic space group $P\bar{1}$ with Z = 2, $F(000)$ = 804 and μ = 0.091 mm^{-1}. The unit cell parameters for (**2**) were refined from 88847 reflections in the monoclinic space group $C2/c$ with Z = 4, $F(000)$ = 392 and μ = 0.098 mm^{-1}. The unit cell parameters for co-crystal (**3**) were refined from 149930 reflections in the triclinic space group $P\bar{1}$ with $Z=2$, $F(000)$ = 956 and μ = 0.097 mm^{-1}. No absorption or extinction corrections were applied to the data. Refer to Table 1 for selected crystallographic information from the independent atom model (IAM) and multipole (*Exp*) refinements.

Table 1: Selected crystallographic information for (1), (2) and (3)

	1	**2**	**3**
Formula	$C_{42}H_{45}N_7O_7$	$C_5H_6N_1O_2$	$C_{48}H_{54}N_8O_{10}$
Molecular Mass	759.85	112.11	902.97
Crystal size (mm^3)	0.3 x 0.2 x 0.25	0.25 x 0.3 x 0.25	0.2 x 0.25 x 0.25
Temperature (K)	150	150	150
Crystal system	Triclinic	Monoclinic	Triclinic
Space group	$P\bar{1}$	C2/c	$P\bar{1}$
a (Å)	8.682(2)	7.093(1)	10.291(1)

b (Å)	14.447(3)	14.004(1)	11.939(1)
c (Å)	15.904(3)	9.686(1)	18.472(2)
α (°)	105.39(3)		85.71(1)
β (°)	90.75(3)	91.40(1)	78.11(1)
γ (°)	92.06(3)		82.22(1)
Volume (Å^3)	1921.50(7)	961.81(2)	2197.82(4)
Z	2	4	2
Refinement Method	Full-matrix least squares on F^2	Full-matrix least squares on F^2	Full-matrix least squares on F^2
No. of reflections collected	291974	88847	149930
No. unique	61577	7796	49537
R_{int}	0.055	0.053	0.063
Completeness (%)	96.2	99.0	96.4
No. reflections used	28783	5753	28802
ρ_c (gcm^{-1})	1.313	1.272	1.364
F(000)	804	392	956
μ (mm^{-1})	0.091	0.098	0.097
sin θ/λ_{max}	1.26	1.25	1.12
θ range for data collection (°)	2.657 - 63.339	2.909 - 62.673	2.502 - 52.572
Index ranges	-18≤*h*≤21 -36≤*k*≤36 -39≤*l*≤39	-17≤*h*≤17 -34≤*k*≤34 -24≤*l*≤24	-22≤*h*≤22 -26≤*k*≤26 -41≤*l*≤41
IAM Refinement			
Final R1, wR2	0.0568, 0.1518	0.0399, 0.1075	0.0388, 0.0678
Goodness of fit	0.918	1.051	0.905
Residual density (*e*Å^{-3})	-0.68 ,0.87	-0.36, 0.52	-0.58, 0.94
Multipole Refinement			
N_{obs}/N_{var}	21.18	32.81	18.67
R(F), R(F^2), all data	0.157, 0.0514	0.061, 0.034	0.061, 0.034
R(F), R(F^2) > 3σ(F)	0.049, 0.042	0.033, 0.032`	0.035, 0.031
Goodness of fit	1.2847	1.7082	2.1857
Residual density (*e*Å^{-3})	-0.18, 0.43	-0.28, 0.18	-0.21, 0.32

Data reduction and refinement strategies

The structures of (**1**), (**2**) and (**3**) were solved using direct methods (SHELXS-2014).[14] In each case, a full-matrix least-squares refinement based on F^2 was performed using SHELXL-2014.[14] The bond lengths between non-hydrogen atoms to hydrogen atoms (X-H bonds, where X=C, O, N) were fixed at average values obtained from neutron diffraction studies, taken from Allen *et al.,*[15] O−H, N−H, and C−H bond lengths being 0.967, 1.009, and 1.083 Å respectively, with bond vectors taken from the original riding H-atom models in the IAM refinement. All non-hydrogen atoms were refined anisotropically.

The coordinates and anisotropic temperature factors from the IAM were then imported into XD,[16] a program that uses a least-squares procedure to refine a rigid pseudo-atom model in the form of the Hansen-Coppens multipole formalism.[17] In this formalism, the electron density, ρ(**r**) within a crystal is described by the summation of aspherical pseudoatoms (each with its own electron density) with nuclear positions $\mathbf{r}_j$ as shown in the Equation (1).

$$\rho(\boldsymbol{r}) = \sum_j \rho_j \left(\boldsymbol{r} - R_j\right) \tag{1}$$

The complete density of the pseudo-atomic model is modelled by Equation (2).

$$\rho_j\left(\boldsymbol{r}_j\right) = P_c\rho_c + \kappa'^3 P_v\rho_v(\kappa'\boldsymbol{r}) + \kappa''^3 \sum_{l=0}^{l_{max}} \sum_{m=-l}^{m=1} P_{lm}R_l\,(\kappa''\boldsymbol{r}_j)d_{lmp}(\theta_j,\phi_j) \tag{2}$$

The expression for the pseudo-atom density includes the usual spherical core, a term to describe the spherical component of the valence density, plus a deformation term describing the asphericity of the valence density. The radial functions $\{R_l(\boldsymbol{r}_j)\}$a are modulated by angular functions $\{d_{lmp}(\theta_j\,,\,\phi_j)\}$ defined by axes centred on each atom. A number of radial functions may be used, the most common being Slater-type functions given in Equation (3).

$$R_l(\boldsymbol{r}) = Nr^{nl}\exp(-\varsigma_l \boldsymbol{r}) \quad (3)$$

The multipole refinement process began with an analysis of the results of higher order spherical atom refinement (usually sin θ/λ > 0.7 A^{-1}), providing accurate atomic positions and temperature factors forming the basis for the remainder of the refinement. The refinement was performed by introducing the multipole expansion in a stepwise manner, ultimately being truncated at the octapole level (l_{max} = 3) for C, O and N. Each C, O and N atom was assigned a kappa prime (κ′, a spherical function which governs 3D directional expansion/contraction of the valence shell) during the refinement to allow for accurate modelling of electron density, and finally a κ′′ value, which models radial expansion/contraction of the valence electrons. The density of hydrogen atoms was modelled using a single monopole, with κ′ fixed at 1.2, with the aspherical density modelled by a single bond-directed dipole (l_{max} = 1). The refinements were continued until convergence was reached for each multipole level before the next one was introduced. The Hirshfeld rigid bond test was used to determine if the anisotropic displacement parameters were of any actual physical significance; *i.e.*, the electron density was successfully deconvoluted from the inherent thermal smearing[18]. This test measures the differences in mean-squared displacement amplitudes (DMSDA) with ADPs deemed to be described as physically meaningful if they are below 1 x 10^{-3} $Å^2$. The average value obtained from these refinements is 5 x 10^{-5} $Å^2$, 1 x 10^{-4} $Å^2$ and 6 x 10^{-5} $Å^2$ for (**1**), (**2**) and (**3**) respectively. Scale and temperature factors were refined separately from the multipole models described above, except in the final refinement cycles, where the full variance-covariance matrix is needed to get meaningful standard uncertainties (su). In all cases, reflections were required to have an intensity of $F > 3\sigma(F)$ to be included in the refinement. This model is termed *Exp* in the remainder of the manuscript.

Computational Methods

Gas phase, single point (SP) calculations were performed on (**1**), (**2**) and (**3**) with the geometry taken from the high-order experimental coordinates. Geometry optimisation (OPT) as well as SP calculations were also performed on all structures. All theoretical calculations were performed with the Gaussian 09 suite[19] at the 6-31+G(d,p) level of theory for all structures. All calculations used the three-parameter hybrid exchange function developed by Becke[20] in conjunction (*vide supra*) with the exchange correlation potential, corrected *via* gradient developed by Lee *et al.*[21] together with the long range dispersion correction proposed by Tawada *et al.*[22-23] (CAM-B3LYP). Analysis of the topology of electron density from the experimental model was performed using the XDPROP portion of XD,[16] while analysis of the electron density for the theoretical densities was performed using the AIMALL[24] package.

Discussion

Geometry

Bond lengths and angles for all experimental structures were obtained from the multipole model refinement output, while bond lengths for the theoretical structures were obtained from DFT optimisation[19]. For (**1**) and (**3**), the X-ray structure was in excellent agreement with results reported by Chang *et al.*[4] with mean differences in bond lengths and angles of 0.009 Å and 0.2° for (**1**) and 0.008 Å and 0.2°for (**3**). A similar situation was seen for (**2**) with mean differences of 0.004 Å and 0.02° when compared to the high resolution structure published by Craven *et al.*[25]. The geometry of the *Exp* model was also in good agreement with that obtained from the OPT calculation with mean differences in bond lengths and angles of

0.002Å and 0.5°, 0.001 Å and 0.01° and 0.004Å and 0.2° for (**1**), (**2**) and (**3**) respectively. A comparison of the experimental geometry between the macrocycle and barbital molecules in (**1**) and (**2**) and their complex in (**3**) shows they are in excellent agreement with the macrocycle only differing in bond length and angles for 0.002 Å and 0.01° and the barbital differing on average by 0.02 Å and 0.01°. Refer to tables S4-S21 in the supplementary information for a full list of bond lengths and angles.

Interestingly, a visual comparison of the geometry and shape of the macrocycle in (**1**) and (**3**) shows the amide bond O(6)-C(38)-N(6)-H(06) being rotated by 180°, as also mentioned above, with the C=O and N-H bonds facing internally in (**1**) and (**3**) respectively. There was minimal difference in the C(2)-C(38)-N(6)-C(37) torsion angle with values of 169.26° and 170.53° for (**1**) and (**3**) respectively, however a large difference was found in the O(6)-C(38)-N(6)-H(06) torsion angle with values for -178.09° and 166.26° highlighting a large conformational difference between the two amide groups as a result of hydrogen bonding. In both cases, O(6) forms a hydrogen bond with the hydroxyl hydrogen on ethanol, unsurprising as it is the most available hydrogen bond acceptor. However, H(06) is only involved in hydrogen bonding in (**3**) with the intraannular barbital molecule resulting in the more planar conformation of the amide bond in (**3**). This is further discussed in topological analysis of hydrogen bonds.

Toplological Analysis

Topological analysis of the *Exp*, SP and OPT models were carried out and completeness of the analysis was ensured *via* satisfaction of the Morse and Poincaré-Hopf equations[26] for the *Exp* and theoretical models respectively. There was good agreement between all three refinement models for ρ_{bcp} and $\nabla^2\rho_{bcp}$. For ρ_{bcp}, mean differences of 0.03,

0.12 and 0.03 eÅ^{-3} were reported for (**1**), (**2**) and (**3**) respectively. For $\nabla^2\rho_{bcp}$, mean differences of 4.46, 2.51 and 2.95 eÅ^{-5} were reported. A full list of critical points found for (**1**), (**2**) and (**3**) can be found in the Supplementary Information Table S22 – S27.

Hydrogen Bonds

A total of 16, 1 and 17 hydrogen bonds were discovered from topological analysis of (**1**), (**2**) and (**3**) respectively. The bonds consisted of those which contain traditional donors and acceptors such as N – H and O – H to O and N, and those which also contained C - H as a donor. Geometrical details of the bonds can be found in the supplementary information Tables S28 – S30. Geometric analysis of the hydrogen bonds found in (**1**) showed no notable relationships between the type of bond and hydrogen-acceptor length, donor-acceptor length or bond angle. Similar analysis of (**3**) found that O…H bonds have longer hydrogen to acceptor distances compared to N…H bonds, however the small number of the latter type of bond (**2**) may bring this conclusion to doubt. Hydrogen -hydrogen bonds as described by Bader *et al.*[27], were also found in the structures of (**1**) and (**3**) with 4 bonds found in each. In both cases, most hydrogen bonds were directed towards the centre of the ring, somewhat unsurprisingly considering the direction of the amine and amide hydrogens within the macrocycle.

According to Koch *et al.*[28], hydrogen bonds are characterized by relatively low ρ_{bcp} and positive $\nabla^2\rho_{bcp}$. Topological analysis of the hydrogen bonds was carried out for the MM model, while DFT was also used to analyse the intramolecular bonds in (**1**) and (**3**). A total of 8 and 15 intramolecular hydrogen bonds were found in (**1**) and (**3**) respectively.

The binding energies of the hydrogen bonds were calculated by applying the method developed by Abramov[29] and Espinosa[30-31], which utilizes ρ_{bcp} and $\nabla^2\rho_{bcp}$ to estimate the kinetic, potential and total energy density within any given bond and subsequently provide an estimation of the strength of the bond. The ratio –G/V can also be used to estimate covalency in H-bonds: a value of between 0.5 and 1 indicates partly covalent character, while a value of greater than 1 is considered to be purely non-covalent[30]. H-bonds can be separated into three groups by their strengths; weak H-bonds (E_{HB} < 20 kJ mol^{-1}), moderate strength H-bonds (E_{HB} = 20-40 kJ mol^{-1}) and strong H-bonds (E_{HB} > 60 kJ mol^{-1})[32]. Details of the hydrogen bonds as determined by topological analysis for (**3**) are reported in Table 2 while similar tables for (**1**) and (**2**) can be found in the Supplementary Information Tables S31 and S32 respectively.

A comparison of the bond strengths calculated between experiment and theory for (**1**) and (**3**) found that they were in relatively good agreement with mean differences of approximately 5 kJ mol^{-1} and 1.5 kJ mol^{-1} respectively. In (**1**), 4 of the hydrogen bonds were found to be weak bonds, 12 were found to be of moderate strength and one strong bond (54.5 kJ mol^{-1}) was found. The location of this strong bond between a macrocyclic oxygen and the hydroxyl hydrogen on the ethanol (O(001)-H(001)…O(6)) is the primary interaction which holds the ethanol molecule in the centre of the ring. As a result, the strength of the bond is unsurprising.

Both (**1**) and (**3**) contain macrocycle-macrocycle intramolecular interactions and these play an important role in maintaining the conformation of the ring in both complexes. All of these interactions in both complexes are of the form C-H⋯O. These hydrogen bonds all involve aromatic carbon atoms as donors and the carbonyl oxygen on the amide groups as acceptors. The bonds are conserved between (**1**) and (**3**) with an extra bond C(36)-H(36)⋯O(6) found in (**3**) due to the rotation of the amide group centred on N(6) as discussed above. The

geometries of the analogous bonds are very similar with all bonds exhibiting donor to acceptor distances of ~2.8 Å and donor-hydrogen-acceptor (DHA) bond angle in the range of 110-120°. The largest differences in DHA bond angles were seen for the C(11)-H(11)···O(2) and C(34)-H(34)···O(5) bonds which had angles of 118.4 and 110.1° in (**1**) and values if 111.0 and 116.4° in (**3**). These minor differences can be attributed to the hydrogen bonding involving the amide hydrogens. H(03) and H(04) respectively. In (**1**), the H(04) atoms is bound to the intraannular ethanol and H(03) is involved in intermolecular bonding while in (**3**), both atoms are involved in hydrogen bonding with the barbital molecule. A similar situation is seen in a comparison of bond strengths, with all analogous bonds being categorized as moderate strength and the extra bond in (**3**) being considered strong (54.5 $kJmol^{-1}$). Minor differecnes in bond strength were seen in the C(9)-H(9)···O(1) and C(11)-H(11)···O(2) bonds by approximately 10 and 7 $kJmol^{-1}$ and these can be attributed to the different environments these atoms are located in between (**1**) and (**3**).

In the complex (**3**), 7 hydrogen bonds were found to be weak interactions, 7 were found to be of moderate strength and the remainder were strong bonds. One of the other strongest bonds in (**3**), was in a position analogous to that found in (**1**), between a macrocyclic amide oxygen and hydroxyl hydrogen on ethanol, with the conformation also appearing to be very similar as the amide has been rotated by approximately 180° in (**1**). This conformation was presumably prevented in (**3**) due to the interactions with barbital in the centre of the ring and is further stabilized *via* the formation of the intramolecular bond C(36)-H(36)···O(6) bond with strength of 54.47 $kJmol^{-1}$. The bonds found in (**1**) and (**3**) are one of the strongest bonds within their respective structures and lends credence to the hypotheses mentioned previously that the ethanol plays a primary role in the rotation of the amide by 180° with the ethanol being pushed outside the ring in (**3**) due to the barbital having more

interactions with the macrocycle results in a more thermodynamically stable and hence preferred structure.

Further analysis of the locations of the bonds and their strength in (**3**) showed that the barbital was held in the centre of the ring by many weak and moderate strength interactions rather than a few strong ones. O(1'), O(2') and O(3') located on barbital were heavily involved in hydrogen bonding. O(1') forms a trifurcated hydrogen bond with H(1), H(01)and H(06) with bond strengths of 23.34, 19.45 and 19.45 kJ mol^{-1} respectively. Figures 4a and b shows the Laplacian and deformation density maps for O(1') respectively and the lone pairs can be seen to be clearly polarised towards H(01) and H(06). Interestingly, the strongest bond is C(1)-H(1)···O(1'), as opposed to the remaining two which have N as the donor. The lack of lone pair polarization towards H(1) as seen in Figure 4 would suggest the geometry of the hydrogen bond plays a role in contributing to its binding energy. The hydrogen and donor to acceptor distances for the bond are the shortest of the three while the DHA bond angle is significantly less linear compared to the other two bonds (127.7° compared to 165.3 and 171.3°). This would suggest the distance between donor and acceptor atoms in a hydrogen bond are also contributing factors towards the bond dissociation energy.

Atoms O(2') and O(3') are also heavily involved in hydrogen bonding with O(2') forming four hydrogen bonds; two with the macrocycle in the asymmetric unit with H(14A) and H(03) and two with another macrocycle in another asymmetric unit with H(29A) and H(31A). The bonds with H(03') and H(14A) within the asymmetric unit have DHA angles of 99.7 and 121.8° respectively and both have a strength of 11.67 $kJmol^{-1}$. This is in contract to the two hydrogen bonds formed with H(31A) and H(29A) outside of the asymmetric unit which have DHA angles of 158.0 and 142.3° respectively and strengths of 15.56 and 4.60 $kJmol^{-1}$. The less linear DHA angle values may be due to buckling of the ring and barbital molecules and unsurprisingly, the donor to acceptor distance of these two hydrogen bonds are

shorter. O(3') is involved in two hydrogen bonds. The bonds with H(04) is strong (66.14 kJ mol^{-1}) while the intermolecular hydrogen bond formed with H(19) is weak (7.78 kJ mol^{-1}). The disparity in strength between these two bonds can be attributed to the significantly shorter donor and hydrogen to acceptor distances of the N(4)-H(04)···O(3') bond (2.816 and 1.835 Å respectively) compared to C(19)-H(19)···O(3') (3.451 and 2.569 Å respectively) and the former bond being much more linear with a DHA angle value of 163.1° compared to 138.3°.

These two oxygen atoms on opposing sides of the barbital molecule play a key role in anchoring the barbital molecule to the centre of the macrocycle. The strong hydrogen bonds formed by O(3') play a main role while the weaker bonds formed by O(2') help to stabilise the interaction. Additionally, the weak intermolecular bonds formed by both atoms help to maintain the packing within the crystal lattice. Figures 5a and b show topological maps of O(3'). The lone pair directed towards the macrocycle is significantly more polarised than its counterpart aimed at the weaker interaction with H(19) and helps to explain the significant disparity in bond strength. Atoms H(B1) and H(B2) also formed moderate strength hydrogen bonds (38.91 kJ mol^{-1}) with N(2) and N(5) respectively and these interactions further helped to stabilise the barbital molecule within the macrocycle.

Table 2: Topological analysis of hydrogen bonding in (**3**). Standard uncertainties have been omitted for clarity. They are closely scattered around 0.02 eÅ^{-3} (ρ_{bcp}) and 0.05 eÅ^{-5} ($\nabla^2\rho_{bcp}$).

	ρ	$\nabla^2\rho$	ε	$d_{H\cdots bcp}$	$d_{A\cdots bcp}$	G	V	H	E_{HB}
	/eÅ^{-3}	/eÅ^{-5}		(Å)	(Å)	/E$_h$ eÅ^{-3}	/E$_h$ eÅ^{-3}	/E$_h$ eÅ^{-3}	/ kJ mol^{-1}
Intramolecular									
Macrocycle – macrocycle interactions									
C(9)-H(9)···O(1)	0.159	2.11	0.04	0.885	1.260	0.14	-0.12	0.01	46.69
C(11)-H(11)···O(2)	0.121	1.51	0.33	1.038	1.333	0.09	-0.08	0.01	31.12
C(34)-H(34)···O(5)	0.116	1.50	0.15	0.988	1.331	0.09	-0.08	0.01	31.12
C(36)-H(36)···O(6)	0.169	2.30	0.02	0.836	1.253	0.15	-0.14	0.01	54.47
Macrocycle – barbital interactions									
N(1')-H(B1)···N(2)	0.114	2.32	0.05	0.699	1.358	0.13	-0.10	0.03	38.91
N(2')-H(B2)···N(5)	0.111	2.61	0.02	0.663	1.356	0.14	-0.10	0.04	38.91
N(4)-H(04)···O(3')	0.185	3.08	0.01	0.645	1.195	0.19	-0.17	0.02	66.14
N(1)-H(01)···O(1')	0.079	1.23	0.09	0.856	1.376	0.07	-0.05	0.02	19.45
N(6)-H(06)···O(1')	0.076	1.23	0.12	0.850	1.390	0.07	-0.05	0.02	19.45
C(1)-H(1)···O(1')	0.097	1.31	0.16	0.965	1.327	0.08	-0.06	0.01	23.34
N(3)-H(03)···O(2')	0.066	0.86	0.28	1.350	1.442	0.05	-0.03	0.01	11.67
C(14)-H(14A)···O(2')	0.054	0.66	1.00	1.212	1.472	0.04	-0.03	0.01	11.67
Macrocycle – ethanol interactions									
O(1S)-H(OS1)···O(6)	0.157	4.99	0.06	0.609	1.182	0.27	-0.19	0.08	73.92
Intermolecular									
C(19)-H(19)···O(3')$^{\#a}$	0.036	0.535	0.32	1.128	1.517	0.03	-0.02	0.01	7.78
C(31)-H(31A)···O(2')$^{\#b}$	0.055	1.105	0.15	0.904	1.410	0.06	-0.04	0.02	15.56
N(3)-H(03)···O(1S)$^{\#a}$	0.195	2.642	0.04	0.674	1.189	0.18	-0.17	0.01	66.14
C(29)-H(29A)···O(2')$^{\#b}$	0.023	0.38	0.29	1.092	1.637	0.02	-0.01	0.01	4.6

$^{\#}$Symmetry operators used to define atoms: ^{a}x, y-1, z; ^{b}x+1, y, z

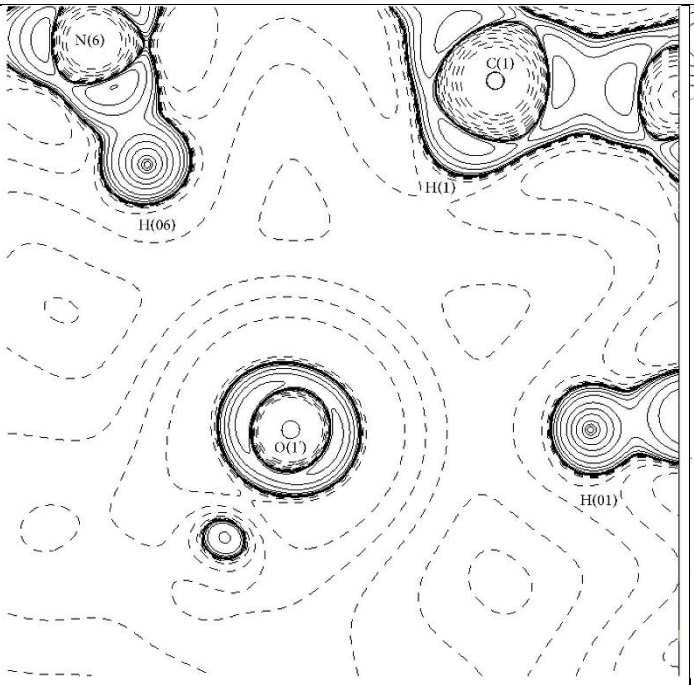

(a)

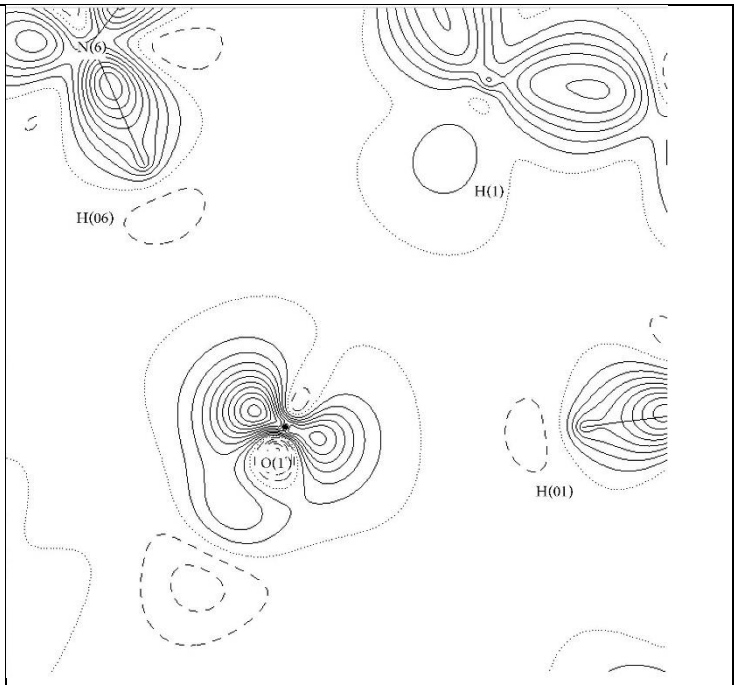

(b)

Figure 4: $-\nabla^2\rho_{bcp}$ and deformation density diagrams showing the trifurcated O(1') atom in hydrogen bonding in (**3**).

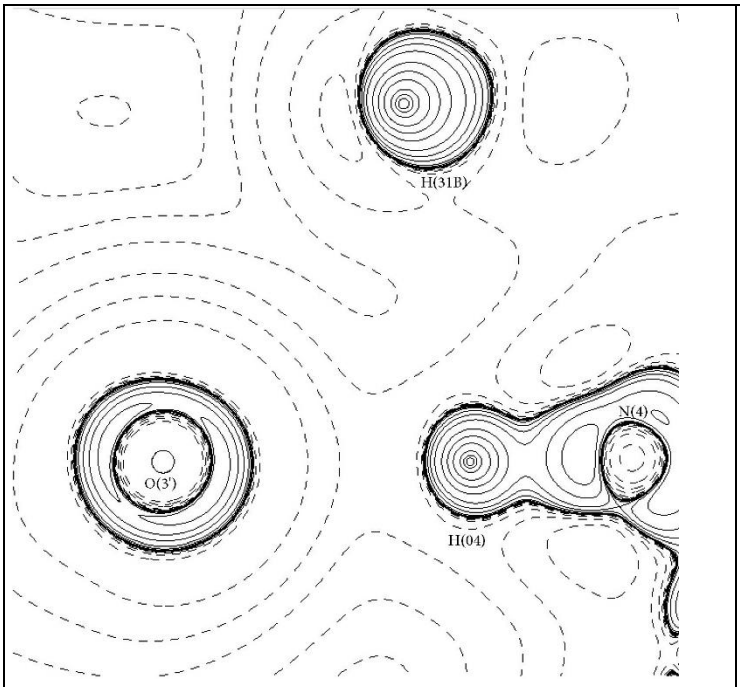

(a)

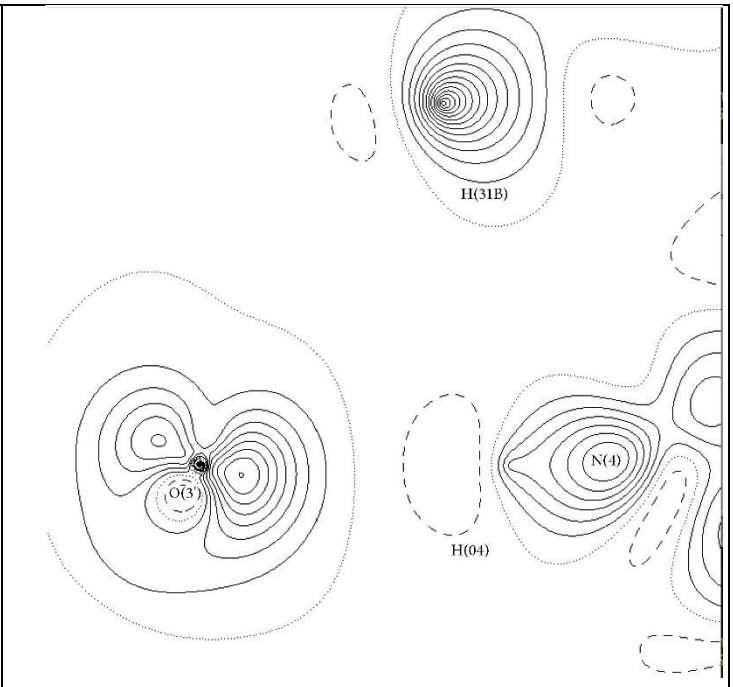

(b)

Figure 5: $-\nabla^2\rho_{bcp}$ and deformation density diagrams showing O(3') involved in hydrogen bonding in (**3**).

Hirshfeld surfaces

Three dimensional Hirshfeld surfaces and corresponding two dimensional fingerprint plots were generated using the CrystalExplorer program [33]. The Hirshfeld surface first introduced by Spackman[34] is a method to represent the electron density around a molecule by utilising the stockholder partitioning scheme originally introduced by Hirshfeld[35]. It should be noted that these surfaces are calculated from the IAM density as opposed to a charge density distribution. As a result, conclusions drawn from these surfaces regarding the types of weak interactions present may not be in complete agreement with those obtained in topological analysis as discussed above. Nevertheless, the Hirshfeld surfaces and associated fingerprint plots provides valuable information regarding the types of interactions present within a system. Hirshfeld surfaces allow visualisation of the space occupied by the electron density based on the van Der waals radii. $\boldsymbol{d_i}$ refers to the distance from the surface to the closest nucleus within the surface while $\boldsymbol{d_e}$ refers to the same distance to the closest nucleus outside the surface. The red regions on the surface represent areas where weak interactions are most likely to form. Figures 6a and b show anterior and posterior views of the Hirshfeld surfaces for (**1**). Similarly, Figures 7a and b shows anterior and posterior views of the Hirshfeld surface for (**3**). Hirshfeld surfaces for (**2**) can be found in Supplementary Information Figure S7. In Figure 6a, the red regions within the macrocycle are located on regions where the ethanolic oxygen interacts with the nitrogen atoms. Figure 7a shows a similar situation, however the higher degree of complementarity between barbital and macrocyle is reflected in the red regions on the macrocycle's Hirshfeld surface surrounding the barbital ring corresponding to the macrocycle-barbital hydrogen bonds discussed above. Fingerprint plots of all systems was also generated and detailed plots for (**1**) and (**3**) can be found in Figures 8 and 9. Fingerprint plots for (**2**) can be found in the Supplementary Information Figure S8. For (**1**), O···H and N···H interactions accounted for 15.1 and 8.6% of

all weak interactions present and is in accordance with the hydrogen bonds reported above. The remaining C···C, C···H and H···H interactions dominated the weak interactions present in the form of dispersive interactions and is attributed to crystal packing where the rings are stacked on top of each other. Analysis of the fingerprint plots of (**3**) found similarities to (**1**) with all interactions contributing similar amount except for N···H interactions. Interestingly, the N···H interactions account for less interactions in (**3**) compared to (**1**) (4.1% vs 8.6% respectively) even though there appears to be more of these interactions in (**3**) due to the complementarity between the barbital molecule and macrocycle. This may be due to the extra interactions formed by nitrile N(01) in (**1**). In (**2**), O···H and H···H interactions accounted for most weak interactions contributing to 45.2 and 50.1% of the fingerprint plots respectively and is attributed to the intermolecular hydrogen bond and the anti-parallel packing in the crystal lattice. The analogous plots for (**2**) can be found in the supplementary information Figures S8a-e.

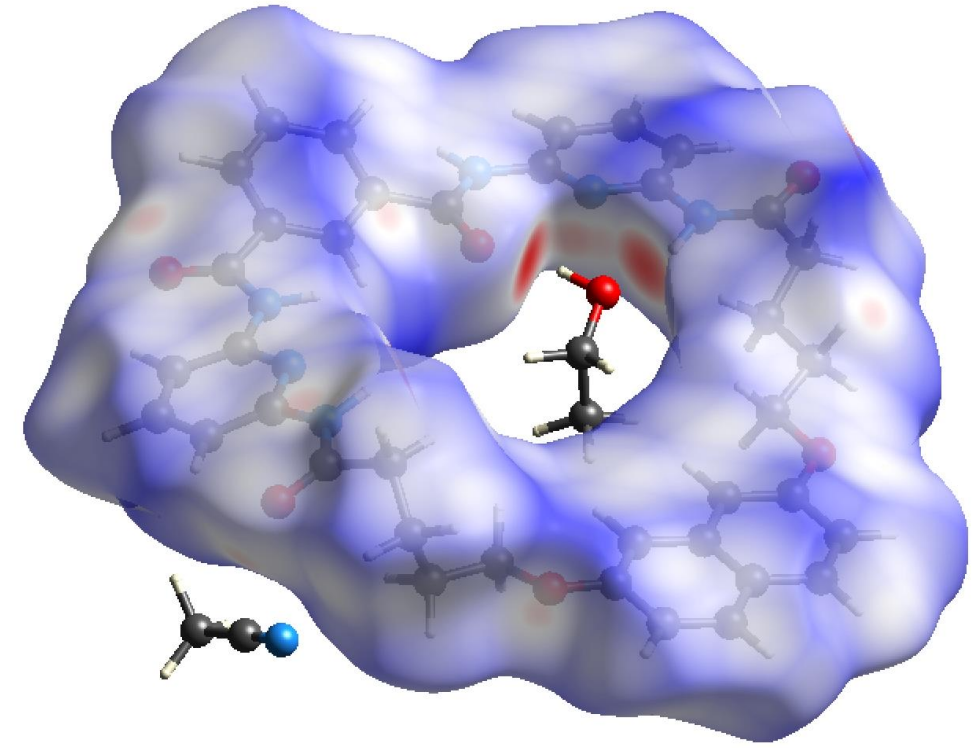

(a)

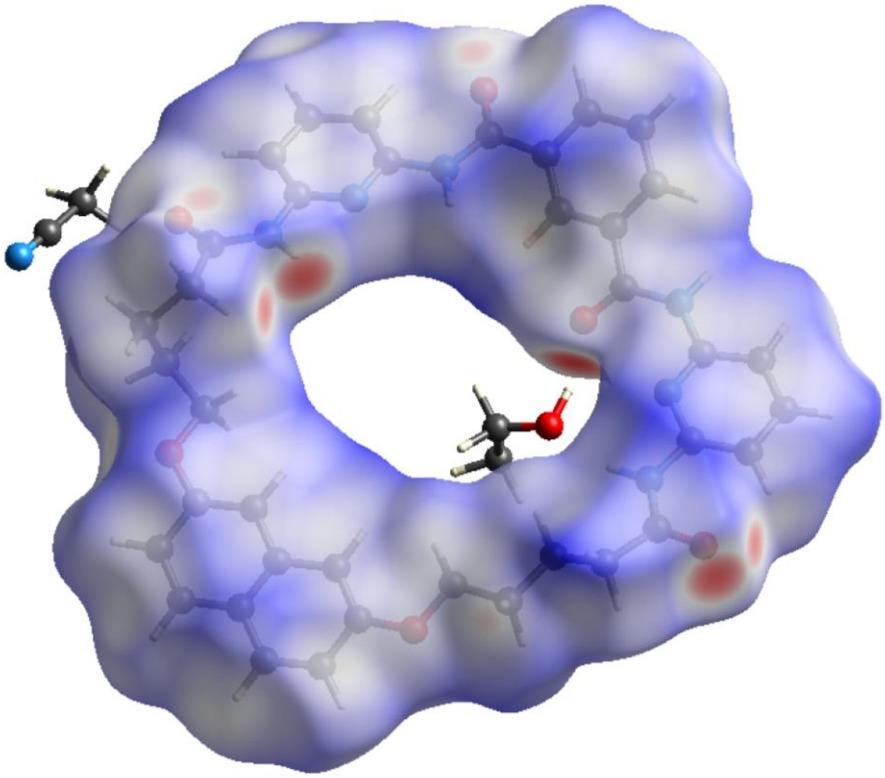

(b)

Figure 6: Hirshfeld surface for (**1**).

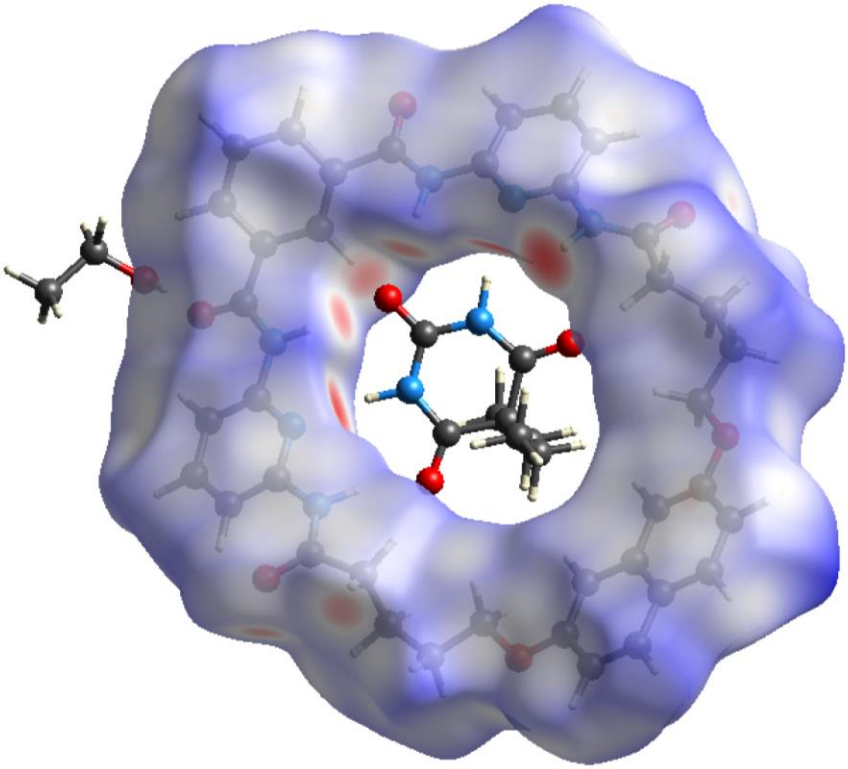

(a)

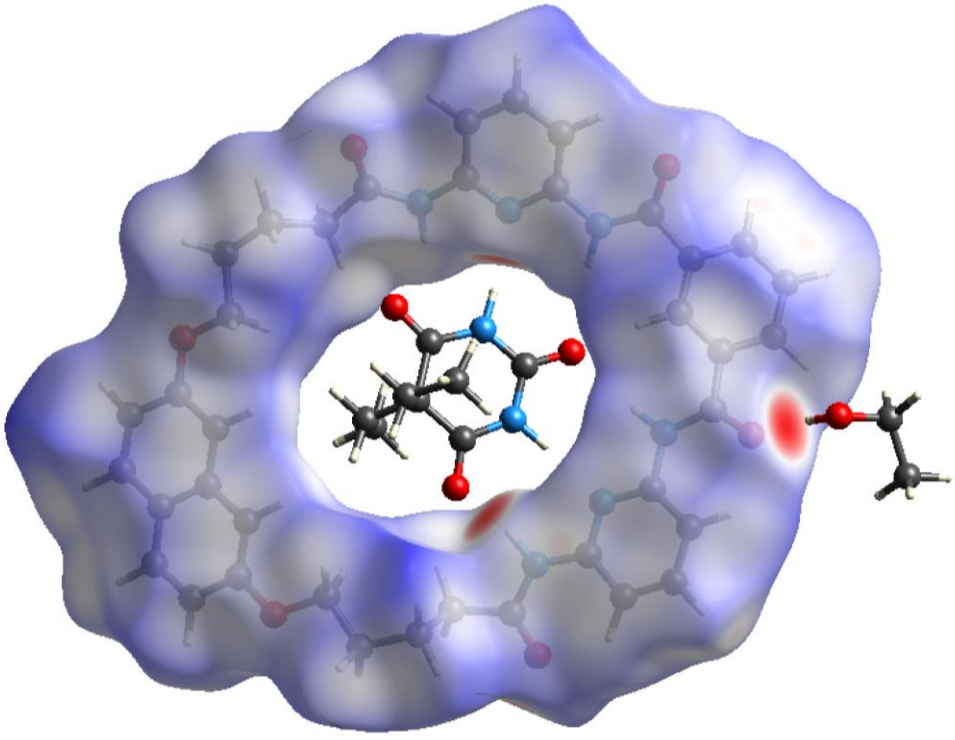

(b)

Figure 7: Hirshfeld surface for (**3**).

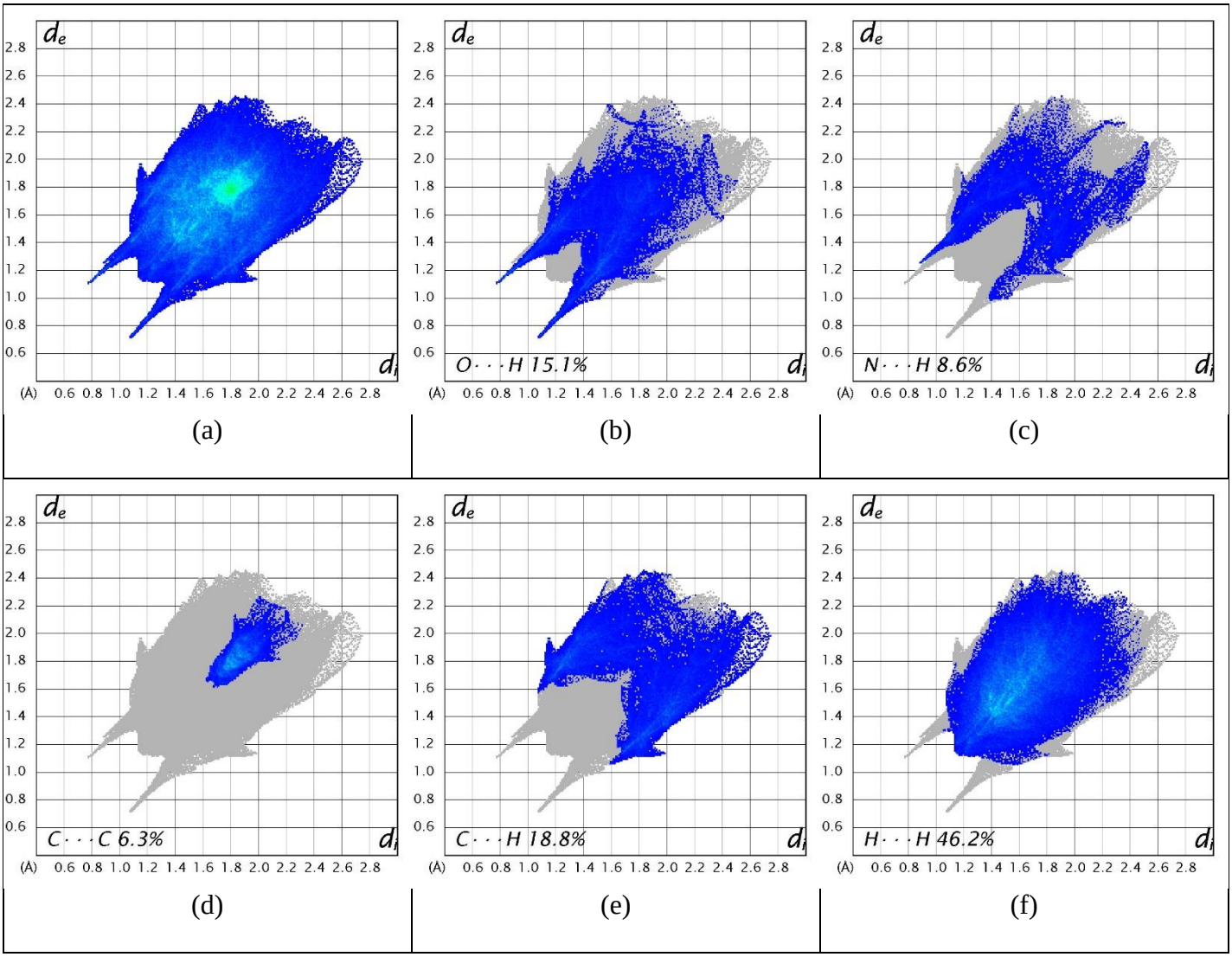

Figure 8: 2-dimensional fingerprint plots of (**1**); (a) all interactions, (b) O···H interactions, (c) N···H interactions, (d) C···C interactions, (e) C···H interactions and (f) H···H interactions

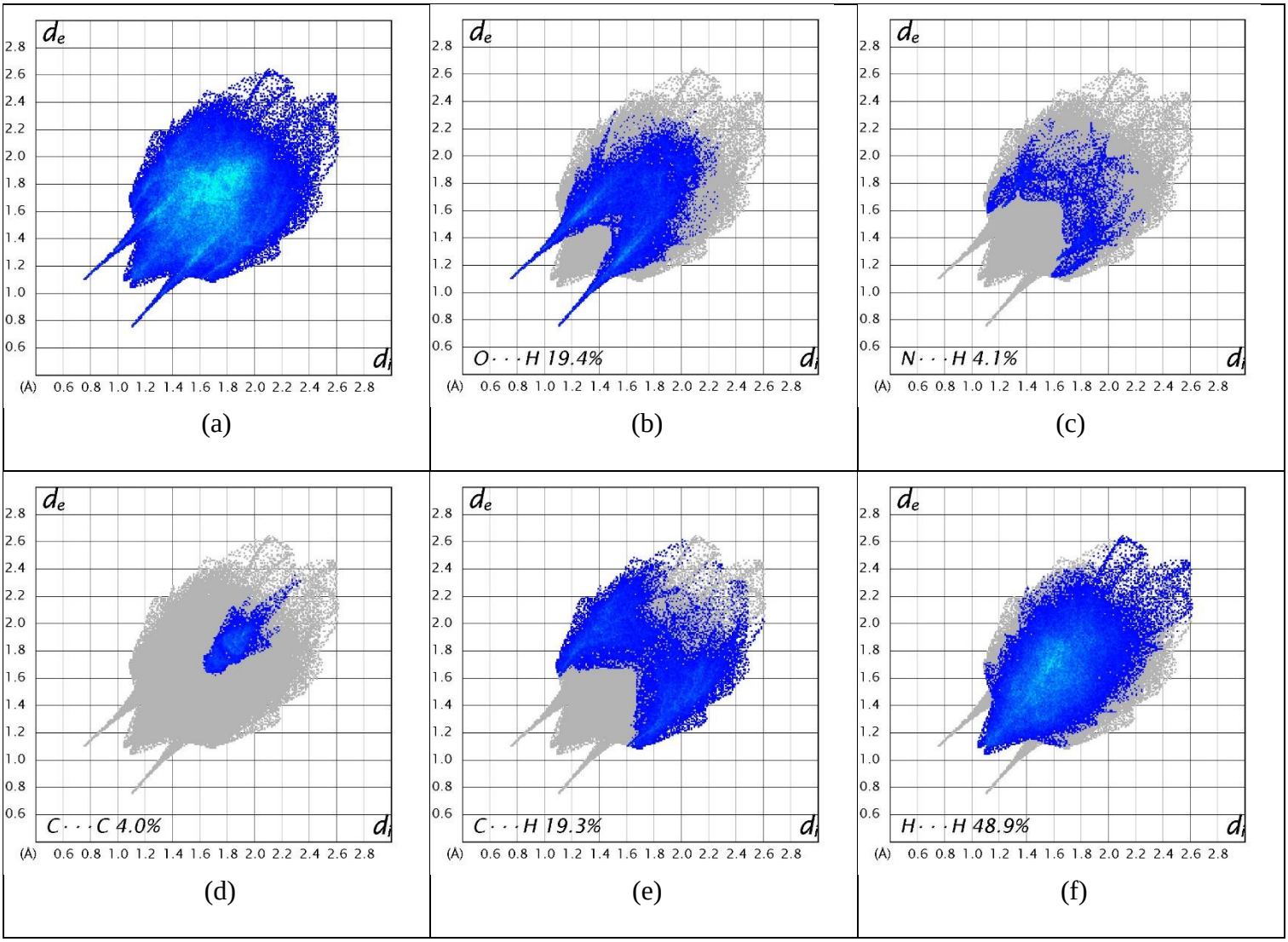

Figure 9: 2-dimensional fingerprint plots of (**3**); (a) all interactions, (b) O···H interactions, (c) N···H interactions, (d) C···C interactions and (e) C···H interactions and (f) H···H interactions

Atomic Charges

Atomic charges obtained *via* integration over atomic basins were also determined in (**1**), (**2**) and (**3**) at the end of the multipole refinement for the *Exp* model and in the SP model. The average difference in the atomic charge between the two models was very low for all structures with mean differences of 0.0002e, 0.02e and 0.04e respectively. The greatest difference between the *Exp* and SP models in (**1**) was found in the C(001) and C(002) atoms with differences of 0.81 and 0.74e respectively. Analysis of the packing motif of (**1**) reveals macrocycle rings to be stacked on top of each other and the C(002) methyl group perpendicular to the plane extending towards the stacked macrocylic ring. Dispersion forces present in the periodic structure, which are absent in the gas phase structure account for the differences in charge.

There was no significant difference in atomic charges between the macrocycle and barbital molecules in (**3**) and their isolated molecules in (**1**) and (**2**) and do not warrant further discussion. The largest difference in charges in the macrocycle were found for C(9), N(2), N(5) and C(31) with each pair having a difference of 0.3e. These are attributed to redistribution of charge due to the atoms in question of their neighbours being involved in weak interactions, occurring more extensively in (**3**) compared to (**1**). N(2) and N(5) are heavily involved in hydrogen bonding in (**3**), forming moderate strength bonds, while N(5) in (**1**) is involved in a much weaker bond. This is also seen through the charge for the two N atoms becoming more negative from (**1**) to (**3**), reflecting the increased rho to form the hydrogen bond. The differences observed in C(9) and C(31) are due to a follow on effect as electrons are redistributed within the aromatic ring and along the chain, reflected in their charges becoming less negative. A similar situation is seen in the comparison of the barbital molecule with the largest difference in C(4’), attributed to O(3’) drawing electrons towards

the N(4)-H(04)…O(3') bond which was found to be a strong hydrogen bond. Complete tables of atomic charges can be found in the supplementary information in Tables S33 and S34.

It has been noted that atomic charges are not very sensitive when used to compare analogous molecules as is the case here due to differences in the shape of the atomic basin among other thing. As such, a comparison of the molecular dipole moments (MDM) which examines the charge separation across a molecule was also carries out on the complexes discussed here. Significant differences in the MDM were found for the macrocycle between (**1**) and (**3**) with values of μ=12.94 and 48.09D respectively. The MDM of the barbital molecule only changed slightly between (**2**) and (**3**) with μ=4047 and 6.55D respectively. This increase is attributed to barbital forming more hydrogen bonds within the macrocycle. The difference in MDM values of the macrocycle are likely due to the presence of the barbital molecule in (**3**) forming a link between opposing ends of the macrocycle resulting in greater charge separation.

Electrostatic Potential

Molecular electrostatic potential (MEP) diagrams allow the researcher to visualise the changes in atomic charge distribution that occur in crystallization, especially between the single molecules and the complex as is the case here. Figures 10-12 show the molecular electrostatic potential (MEP) calculated from the *Exp* model, which have all been plotted on the same scale for comparability. Visual analysis of Figures 10-12 yields some striking features, with the MEP diagrams of (**1**) and (**2**), having relatively even colour distribution throughout the molecules with the charge being between 0.64-1.2e, while the MEP diagram of (**3**), contrasts significantly showing more negative charge over the whole complex, with the most negative area being approximately -1.1e in the area bound by N(1) and N(6).The

difference in electrostatic potential (ESP) can be attributed to the increased number of weak interactions formed in the complex when compared to the individual substituents, with areas not involved in bonding (the naphthalene system in (3)) showing considerably smaller change in ESP compared to the amide region located on the opposite side of the ring. The charge redistribution in the complex is most obviously seen in the amide -aromatic region in (**3**) located between barbital and ethanol. This area contains the highest concentration of weak interactions of all structures and the area is accordingly the most negative. Although some bonds present in (**3**), can be found between analogous atoms in (**1**), the change in ESP is not as pronounced. Similarly, the three O atoms on the barbital molecule have a positive ESP in (**2**) when compared to (**3**). Both examples highlight the charge redistribution that occurs in co-crystallisation of two substances. The large change in charge distribution pre-and post crystallisation can potentially be utilised in future drug design as a method of controlling selectivity and binding affinity of ligands to protein targets or to detoxification vehicles. MEP diagrams are of great utility in understanding how charge redistribution occurs in complex formation.

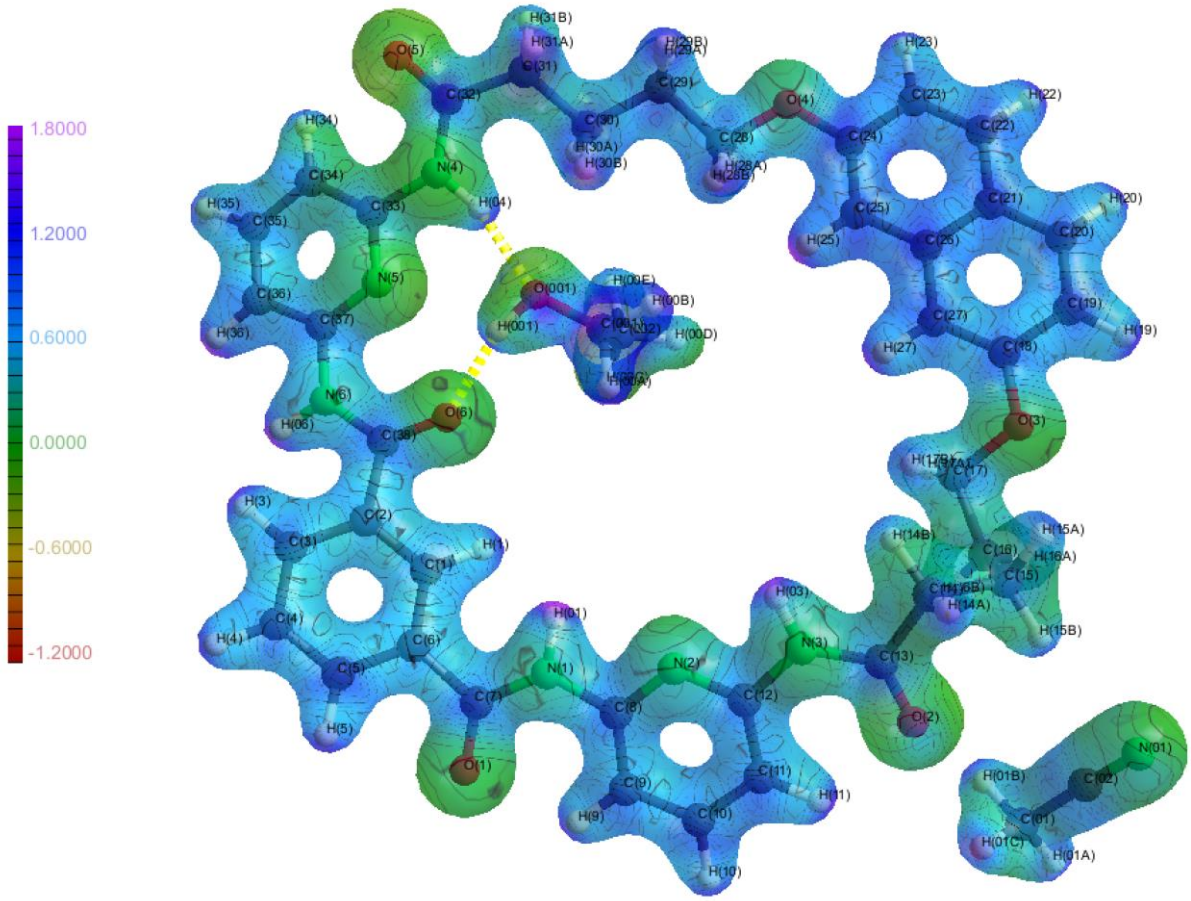

Figure 10: Electrostatic potential of (**1**) plotted on the ρ isosurface[36].

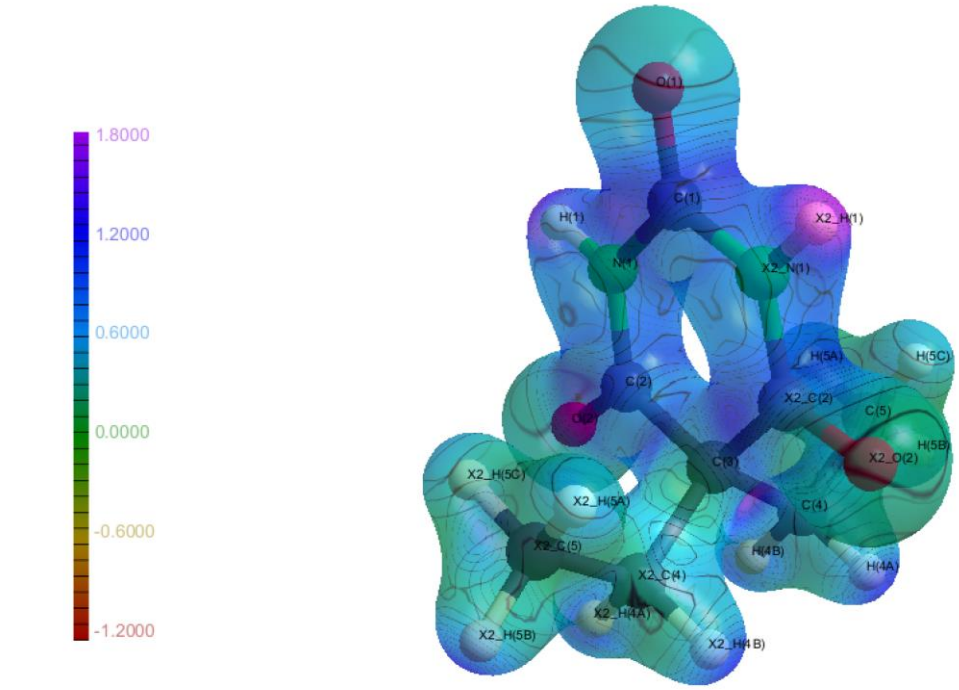

Figure 11: Electrostatic potential of (**2**) plotted on the ρ isosurface[36].

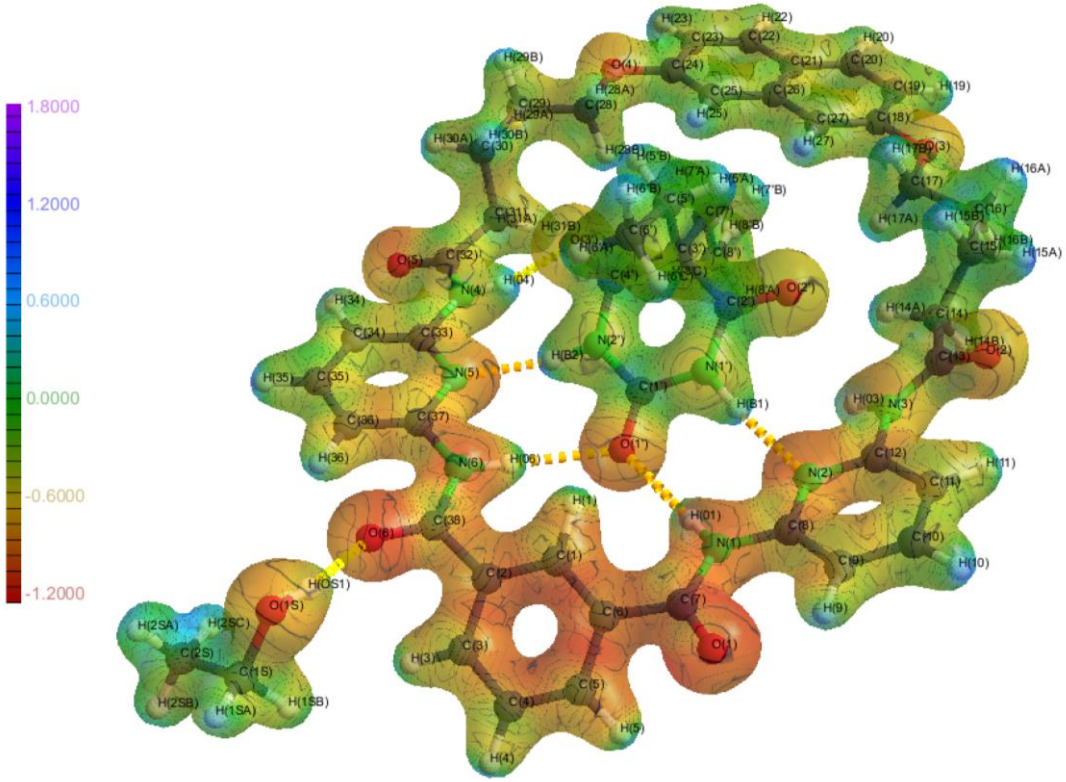

Figure 12: Electrostatic potential of (**3**) plotted on the ρ isosurface[36].

The significant charge redistribution was also examined *via* calculation of lattice energies to gauge the relative stability of (**1**), (**2**) and (**3**). Lattice energies were evaluated using the LATEN option in XD2006, based on total intermolecular interaction energies suggested by Volkov *et al*.[37]. In the *Exp* model, (**1**) was found to be more stable than (**3**) by approximately 20 kJ mol^{-1}. The greater stability of (**1**) in the *Exp* model is expected due to the lack of a compound in the centre of the molecule that needs to also be stabilized while in (**3**), one of the ethyl chains is untethered to the ring and has a high degree of movement.

Conclusion

In this study, experimental charge density studies complemented by quantum mechanical theoretical calculations were carried out to examine the differences between a macrocycle alone and when complexed with barbital in a crystalline state. It was found that the presence of barbital orientated the amide bonds within the macrocycle in a way that optimised the number of hydrogen bonds and other weak interactions that could be formed to stabilise the barbital molecule in the middle of the ring. However, (**3**) was found to be less stable, possible due to an untethered ethyl chain from barbital resulting in a higher degree of movement compared to the ethanol in the middle of the macrocycle in (**1**). Most of these stabilising interactions were hydrogen bonds with strengths ranging from 4-70 kJ mol^{-1}. Further analysis of the electrostatic potential found that significant charge redistribution occurs during co-crystallisation as the macrocycle is reoriented to optimise the number of binding interactions with the guest molecule. These findings have the potential to be applied in future drug design strategies when aiming to control ligand affinity and selectivity.

Supporting information

Spectrosopic data for (**1**) and (**3**), SHADE anisotropic displacement parameters for hydrogen atoms, tables of experimental bond lengths and angles, details of topological analysis, residual density analysis, Hirshfeld surfaces and fingerprint plots. This material is available free of charge via the Internet at http://pubs.acs.org/.

Acknowledgements

DEH and PWG would like to thank The University of Sydney Bridging Support Scheme for funding. JD would like to thank the University of Sydney for an APA scholarship, the Faculty of Pharmacy for research funding and the Sydney Informatics Hub at the University of Sydney for providing access to HPC Artemis. JRH and RV acknowledge support from the NH&MRC. The work was supported by the Danish National Research Foundation (Center for Materials Crystallography, DNRF-93)

References

1. Burdett, J. K., Perspectives in structural chemistry. *Chem. Rev.* **1988,** *88*, 3-30.
2. Marsault, E.; Peterson, M. L., Macrocycles Are Great Cycles: Applications, Opportunities, and Challenges of Synthetic Macrocycles in Drug Discovery. *J. Med. Chem.* **2011,** *54*, 1961-2004.
3. Lipinski, C. A.; Lombardo, F.; Dominy, B. W.; Feeney, P. J., Experimental and computational approaches to estimate solubility and permeability in drug discovery and development settings. *Adv. Drug Delivery Rev.* **2012,** *64, Supplement*, 4-17.
4. Chang, S. K.; Van Engen, D.; Fan, E.; Hamilton, A. D., Hydrogen bonding and molecular recognition: synthetic, complexation, and structural studies on barbiturate binding to an artificial receptor. *J. Am. Chem. Soc.* **1991,** *113*, 7640-5.
5. Nguyen, T. H.; Groundwater, P. W.; Platts, J. A.; Hibbs, D. E., Experimental and Theoretical Charge Density Studies of 8-Hydroxyquinoline Cocrystallized with Salicylic Acid. *J. Phys. Chem. A* **2012,** *116*, 3420-3427.
6. Nguyen, T. H.; Howard, S. T.; Hanrahan, J. R.; Groundwater, P. W.; Platts, J. A.; Hibbs, D. E., Experimental and Theoretical Charge Density Distribution in a Host-Guest System: Synthetic Terephthaloyl Receptor Complexed to Adipic Acid. *J. Phys. Chem. A* **2012,** *116*, 5618-5628.
7. Hibbs, D. E.; Austin-Woods, C. J.; Platts, J. A.; Overgaard, J.; Turner, P., Experimental and theoretical charge density study of the neurotransmitter taurine. *Chem. Eur. J.* **2003,** *9*, 1075-1084.
8. Meents, A.; Dittrich, B.; Johnas, S.; Thome, V.; Weckert, E., Charge-density studies of energetic materials: CL-20 and FOX-7. *Acta Crystallogr., Sect. B: Struct. Sci.* **2008,** *64*, 42-49.
9. Overgaard, J.; Hibbs, D. E., The experimental electron density in polymorphs A and B of the anti-ulcer drug famotidine. *Acta Crystallogr., Sect. A: Found. Crystallogr.* **2004,** *60*, 480-487.
10. Overgaard, J.; Waller, M. P.; Piltz, R.; Platts, J. A.; Emseis, P.; Leverett, P.; Williams, P. A.; Hibbs, D. E., Experimental and theoretical charge density distribution in two ternary cobalt (III) complexes of aromatic amino acids. *J. Phys. Chem. A* **2007,** *111*, 10123-10133.
11. Koritsanszky, T. S.; Coppens, P., Chemical applications of X-ray charge-density analysis. *Chem. Rev.* **2001,** *101*, 1583-1628.
12. Craven, B. M.; Fox, R. O., Jr.; Weber, H. P., The charge density in polymorph II of 5,5-diethylbarbituric acid (barbital) at 198 K. *Acta Crystallogr., Sect. B: Struct. Sci.* **1982,** *B38*, 1942-52.
13. Rigaku Oxford Diffraction. *CrysAlis PRO*. 2017, Rigaku Oxford Diffraction, Yarnton, England
14. Sheldrick, G. M., A short history of SHELX. *Acta Crystallogr., Sect. A: Found. Crystallogr.* **2008,** *64*, 112-122.
15. Allen, F. H.; Kennard, O.; Watson, D. G.; Brammer, L.; Orpen, A. G.; Taylor, R., Tables of bond lengths determined by x-ray and neutron diffraction. Part 1. Bond lengths in organic compounds. *J. Chem. Soc., Perkin Trans. 2* **1987**, S1-S19.
16. Volkov, A.; Macchi, P.; Farrugia, L. J.; Gatti, C.; Mallinson, P.; Richter, T.; Koritsanszky, T. *XD2006 - a computer program for multipole refinement, topological analysis of charge densities and evaluation of intermolecular energies from experimental or theoretical structure factors*, 2006.
17. Hansen, N. K.; Coppens, P., Electron population analysis of accurate diffraction data. VI. Testing aspherical atom refinements on small-molecule data sets. *Acta Crystallogr., Sect. A: Found Crystallogr.* **1978,** *A34*, 909-21.
18. Hirshfeld, F. L., Can x-ray data distinguish bonding effects from vibrational smearing? *Acta Crystallogr., Sect. A: Found. Crystallogr.* **1976,** *A32, Pt. 2*, 239-44.
19. Frisch, M. J.; Trucks, G. W.; Schlegel, H. B.; Scuseria, G. E.; Robb, M. A.; Cheeseman, J. R.; Scalmani, G.; Barone, V.; Mennucci, B.; Petersson *et al*. *Gaussian09*, 2006.
20. Becke, A. D., A new mixing of Hartree-Fock and local-density-functional theories. *J. Chem. Phys.* **1993,** *98*, 1372-7.

21. Lee, C.; Yang, W.; Parr, R. G., Development of the Colle-Salvetti correlation-energy formula into a functional of the electron density. *Phys. Rev. B: Condens. Matter Mater. Phys.* **1988,** *37*, 785-9.
22. Tawada, Y.; Tsuneda, T.; Yanagisawa, S.; Yanai, T.; Hirao, K., A long-range-corrected time-dependent density functional theory. *J. Chem. Phys.* **2004,** *120*, 8425-8433.
23. Yanai, T.; Tew, D. P.; Handy, N. C., A new hybrid exchange–correlation functional using the Coulomb-attenuating method (CAM-B3LYP). *Chem. Phys. Lett.* **2004,** *393*, 51-57.
24. Keith, T. A. *AIMAll*, 14.06.21; TK Gristmill Software: Overland Park KS, USA, 2014.
25. Craven, B. M.; Vizzini, E. A.; Rodrigues, M. M., The crystal structure of two polymorphs of 5,5'-diethylbarbituric acid (barbital). *Acta Crystallogr., Sect. B: Sctruct. Sci.* **1969,** *25*, 1978-1993.
26. Coppens, P., *X-Ray Charge Densities and Chemical Bonding* Oxford University Press New York, 1997.
27. Matta, C. F.; Hernández-Trujillo, J.; Tang, T.-H.; Bader, R. F. W., Hydrogen–Hydrogen Bonding: A Stabilizing Interaction in Molecules and Crystals. *Chem. Eur. J.* **2003,** *9*, 1940-1951.
28. Koch, U.; Popelier, P. L. A., Characterization of C-H-O Hydrogen Bonds on the Basis of the Charge Density. *J. Phys. Chem.* **1995,** *99*, 9747-9754.
29. Abramov, Y. A., On the possibility of kinetic energy density evaluation from the experimental electron-density distribution. *Acta Crystallogr., Sect. A: Found. Crystallogr.* **1997,** *A53*, 264-272.
30. Espinosa, E.; Molins, E.; Lecomte, C., Hydrogen bond strengths revealed by topological analyses of experimentally observed electron densities. *Chem. Phys. Lett.* **1998,** *285*, 170-173.
31. Espinosa, E.; Souhassou, M.; Lachekar, H.; Lecomte, C., Topological analysis of the electron density in hydrogen bonds. *Acta Crystallogr., Sect. B: Struct. Sci.* **1999,** *55*, 563-572.
32. Hibbert, F.; Emsley, J., Hydrogen Bonding and Chemical Reactivity. *Adv. Phys. Org. Chem.* **1990,** *26*, 255-379.
33. Wolff, S.; Grimwood, D.; McKinnon, J.; Turner, M.; Jayatilaka, D.; Spackman, M., Crystal Explorer ver. 3.1. *University of Western Australia, Perth, Australia* **2013**.
34. Spackman, M. A.; Jayatilaka, D., Hirshfeld surface analysis. *CrystEngComm* **2009,** *11*, 19-32.
35. Hirshfeld, F. L., Bonded-atom fragments for describing molecular charge densities. *Theor. Chem. Acc.* **1977,** *44*, 129-138.
36. Hubschle, C. B.; Luger, P., MolIso - a program for colour-mapped iso-surfaces. *J. Appl. Crystallogr.* **2006,** *39*, 901-904.
37. Volkov, A.; Koritsanszky, T.; Coppens, P., Combination of the exact potential and multipole methods (EP/MM) for evaluation of intermolecular electrostatic interaction energies with pseudoatom representation of molecular electron densities. *Chem. Phys. Lett.* **2004,** *391*, 170-175.